Int J Adv Manuf Technol (2017) 89:1173–1192
DOI 10.1007/s00170-016-9148-5

ORIGINAL ARTICLE

Study on force modeling considering size effect in ultrasonic-assisted micro-end grinding of silica glass and Al_2O_3 ceramic

Zhang Jianhua[1] **· Li Hui**[1] **· Zhang Minglu**[1] **· Zhao Yan**[1] **· Wang Liying**[1]

Received: 10 March 2016 / Accepted: 4 July 2016 / Published online: 19 July 2016
© Springer-Verlag London 2016

Abstract Ultrasonic vibration-assisted micro-end grinding (UAMEG) is a promising processing method for micro-parts made of hard and brittle materials. Grinding force is one of the most important parameters which can synthetically reflect the grinding process. So, it is a key issue to establish a model for the reliable prediction of grinding force in UAMEG. First, by studying removal mechanism and the micro-topography of grinding surface, the micro-end grinding zone is divided into the following three grinding regions: main grinding region, plowing grinding region, and sliding grinding region. Then, the single-grain force model is developed under different material removal modes, and the grinding force model of the whole grinding wheel is established considering size effect. To verify the correctness of the proposed model, contrast grinding tests of silica glass with and without ultrasonic assistance using micro-radial electroplated diamond wheel are conducted. The theoretical predicted values of grinding force match well with the experimental results. The grinding forces are significantly reduced, and ductile machining is easier to be achieved.

Keywords Force model · Ultrasonic vibration · Micro-end grinding · Size effect · Ductile machining

1 Introduction

Application of hard and brittle materials in abroad range of industries, such as semiconductor, optics, micro-robot, micro-electronics, and biomedical, has been steadily grown in recent years. These materials, such as glass and ceramics, exhibit many excellent properties, high hardness, superb dimensional stability, high mechanical strength, and prominent thermal, chemical, and wearing resistance [1, 2]. These properties make them very suitable material for manufacturing of precision components such as camera lens, touch screens, wafers, micro-electronic chips, micro-fluidic devices, and micro-molds. Meanwhile, these properties make them difficult to cut. In the cutting of hard and brittle materials with conventional machining conditions, the chip formation is usually a fracture process that damages the machined surface and leads to unacceptable part quality [3].

Micro-grinding is one of the most important processing technologies for machining of micro-parts of hard and brittle materials. Ramesh [4] conducted high-table-reversal-speed micro-grinding tests on different hard and brittle materials, in which fine slots with 0.1-mm width and high aspect ratio of 15 were produced. The lowest surface roughness obtained of WC, Al_2O_3, and BK7 were 0.16, 0.32, and 0.52 μm, respectively. The lowest average surface roughness of 12.97 nm was achieved in Rahman's experiment [5], in which micro-grinding of BK7 glass was carried out using micro-EDM-fabricated PCD tool.

✉ Zhang Jianhua
jhzhang@hebut.edu.cn

Li Hui
lihui2009@hebut.edu.cn

Zhang Minglu
zhangml_hebut@163.com

Zhao Yan
zhaoyan5995@gmail.com

Wang Liying
lywangedu@sina.com

[1] School of Mechanical Engineering, Hebei University of Technology, No. 8 Guangrongdao St., Hongqiao, Tianjin, China

But, there exist several challenges that lie in micro-grinding, high grinding forces, which result in high heat generation, severe surface damage due to brittle fracture, and rapid micro-wheel wear [4, 6, 7]. It has been demonstrated to be an effective method for solving the problems above to assist ultrasonic vibration into machining process. Akbari and Borzoie [8] investigated the ultrasonic vibration effects on grinding process of alumina ceramic by experiments. The tests results also indicated significant improvements; surface roughness improved by 8 %, total grinding force reduced by up to about 22 %, and workpiece fracture strength increased by approximately 10 % on average. Tawakoli and Bahman [9] conducted comparative experiments of ultrasonic-assisted dry grinding and conventional dry grinding of 42CrMo4, which demonstrated considerable advantages of the former technology, significant improvement on the R_z parameter, and up to 60 % reduction of normal grinding force. Chen [10] conducted an experimental study of the effects of ultrasonic vibration on grinding surface roughness, showing that the application of ultrasonic vibration to the grinding process can lower the workpiece surface roughness. In Yan's research [11], comparative grinding experiments on surface quality of nano-ZrO_2 ceramic were carried out using diamond wheel in different condition, both with and without ultrasonic vibration. The results show that the surface quality is improved with ultrasonic assistance compared with conventional diamond grinding. In addition, it is easier for ultrasonic-assisted grinding to achieve material ductile region removal. In Wang and Lin's [12] research on ultrasonic vibration-assisted cylindrical grinding of hard and brittle materials, the models of grinding force and material removal rate were developed and verified according to the test. The result indicated that the grinding force decreased as the amplitude and frequency increased and the roughness decreased first and increased subsequently. But, the force model was developed on the basic assumption that brittle fracture is the primary mechanism of material removal, neglecting material plastic removal. Zhang and Zhao [13, 14] conducted experimental study and preliminary mechanism research on ultrasonic vibration-assisted micro-end grinding (UAMEG) of silica glass. Experimental result shows that grinding forces are significantly reduced (up to 65.6 % of normal grinding force, up to 47.7 % of tangential grinding force, up to 42.2 % of cross-feed directional grinding force) due to the introduction of ultrasonic vibration; the surface quality is significantly improved because of assisted ultrasonic vibration. However, a comprehensive and systematical force model needs further study to investigate the mechanism of grinding force in UAMEG of brittle material.

In recent years, considerable work has been carried out to develop a mathematical model for the grinding force. Hecker and Liang [15] developed the predictive models for grinding force and power based on the probabilistic distribution of undeformed chip thickness as a function of the kinematic conditions, material properties, wheel micro-structure, and dynamic effects. Park and Liang [16] developed a predictive model for the micro-grinding process by combined consideration of mechanical and thermal effects within a single-grit interaction model, while the size effect of micro-machining was incorporated. This model quantitatively predicted micro-grinding forces based on micro-grinding wheel topography and material properties including crystallographic effects. Chang and Wang [17] focused on stochastic nature of the abrasive wheel and tried to establish a force model of the grit distribution on the wheel. But, the identification of the grit density function is difficult, requiring correct assumptions for grit locations. A new grinding force model was developed by Durgumahanti [18] which incorporated the effects of variable coefficient of friction and plowing force. This is based on the fact that chip formation during grinding consists of the following three stages: plowing, cutting, and rubbing. Equations for the total normal and tangential force components per unit width of the grinding, during these three stages, were established. The plowing force components were modeled by performing single-grit tests. Agarwal and Rao [19] built an analytical model to predict the force and power of ceramic grinding based on the undeformed chip thickness. The model was validated by conducting experiments of silicon carbide, which indicated that the proposed model was in good agreement with the experimental data obtained from different kinematic conditions. Cheng and Gong [20] developed a predicting model of grinding force considering crystallographic effects in micro-grinding of single crystal silicon. Ductile-regime transition in micro-grinding process of single crystal silicon was revealed; 20 and 100 nm were turned out to be two critical conditions based on analysis of experiment results. From researching summary of above, it is found that there is not a systematically theory achievement for force prediction in UAMEG. Further research on modeling of grinding force is important and necessary to UAMEG.

In this paper, an analytical model of the grinding force in UAMEG is established considering size effect. The proposed model is based on the material removal mechanism and the micro-topography of grinding surface. In order to verify the correctness of the proposed model and reveal the grinding parameters on grinding forces and surface quality, contrast grinding tests of silica glass with and without ultrasonic assistance using micro-radial electroplated diamond wheel are conducted. The grinding forces are measured using a three-component dynamometer. The surface characteristics are detected using the scanning electron microscope. The experiment results demonstrate that grinding forces are significantly reduced; surface quality is obviously improved due to ultrasonic assistance in UAMEG. The predicted and the measured values of surface roughness are in very good agreement.

2 Mechanism analysis of UAMEG

As shown in Fig. 1a, UAMEG consists of the following three crucial motions: workpiece ultrasonic vibration, which is simple harmonic motion with small amplitude and high frequency; grinding wheel high-speed rotary motion; and high-accuracy micro-feed motion. The coordinate system is defined as follows: the *x* axis is in the direction of wheel precision feed and workpiece ultrasonic vibration; the *y* axis is oriented in cross-feed direction; and the *z* axis is normal to uncut surface and in the direction of cutting depth, around which the grinding wheel rotates at high speed.

For convenience, several hypothesis conditions are put forward in this study; abrasives are well distributed with uniform size, deformation and run out of the wheel are negligible, the wheel end face is parallel to workpiece surface, and ultrasonic amplitude and frequency keep steady in machining process.

It can be detected by microscopic observation of grinded surface that grinding zone between the wheel and material in micro-end grinding is split into the following three grinding regions, as shown in Fig. 1b: chip formation region, plowing region, and sliding region.

1. In chip formation region, abrasives in exterior margin of wheel end face encounter unmachined material and lead to chip formation by fracture crack or shearing formation. There exists a minimum undeformed chip thickness, above which the material can be removed by fracture crack or chip formation.
2. In plowing region, abrasives in inner margin of wheel end face lead plowing effects to the material that is below the minimum undeformed chip thickness. Plastic deformation and pileup of a part of material around the abrasive tip occur in front of and on both sides of the abrasive along scratching groove. When plastic deformation accumulates up to the undeformed chip thickness, material can be removed in form of chip formation. Elastic deformation occurs beneath the abrasive tip in the shape of hemisphere. Then, elastic recovery of material behind the abrasive tip occurs after the abrasive scratched over.
3. In sliding region, there exists no material removal but elastic deformation and elastic recovery.

2.1 Material removal mechanism in grinding region I

As investigated in previous research [14], the instantaneous abrasive cutting thickness (h) is defined as the distance between trajectories of the cutting abrasive and the former abrasive in the direction parallel to the surface. Real abrasive cutting thickness is determined by the trajectories of a quite several adjacent abrasives. For convenience, two adjacent abrasives are taken into account. The geometrical schematic of instantaneous abrasive cutting thickness is shown in Fig. 2 and is mathematically modeled.

The time when the former abrasive (here defined as the i_{th} abrasive) moves to point Q and the cutting abrasive (here defined as the i_{th} + 1st abrasive) moves to point N is defined as start time. t_B is defined as the time when the i_{th} abrasive moves to point B (x_{tB}, y_{tB}) along the dashed line. At the same time, the center of the wheel moves to point O_i. Point A (x_{tA}, y_{tA}) is the intersection of trajectory of the (i + 1)th abrasive and the extension line of l_{BOi}. The (i + 1)th abrasive moves to point A, and the center of the wheel moves to point O_{i+1} at t_A.

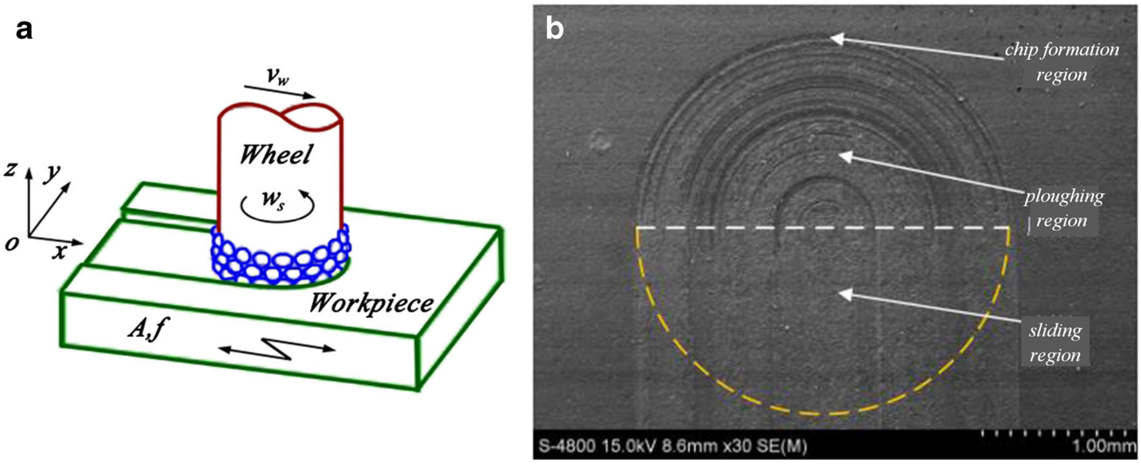

Fig. 1 Schematic diagram of UAMEG. **a** Coordinate system and **b** SEM of grinding surface

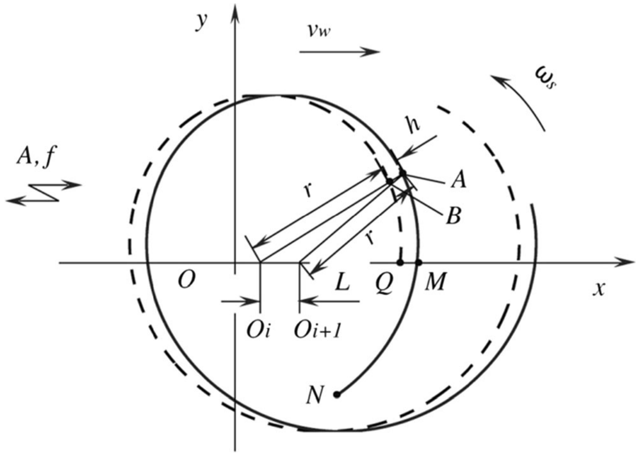

Fig. 2 Geometrical schematic of instantaneous abrasive cutting thickness

Based on the principles of geometry, instantaneous abrasive cutting thickness of the $(i + 1)$th abrasive at t_A can be expressed as

$$h_{i+1}^{t_A} = \sqrt{r^2 + L^2 - 2rL\cos[\omega_s(t_A - \Delta_t)]} - r \tag{1}$$

where $\Delta_t(\Delta_t = 1/mn)$ is defined as the time difference according to the phase difference of these two adjacent abrasives, which is equal to the time that the $(i + 1)$th abrasive moves from point N to point M; m is the quantity of all the abrasives in the most exterior margin of micro-wheel end face; n is the spindle speed; and L is the distance between O_i and O_{i+1}.

$$L = x_{0_{i+1}} - x_{o_i} \tag{2}$$

where $x_{o_i}^{t_B}$ and $x_{o_{i+1}}^{t_A}$ are the x positions of the wheel center at t_B and t_A, respectively, which can be further expressed as

$$\begin{cases} x_{O_{i+1}}^{t_A} = v_w \cdot t_A + A \cdot \sin(\omega_f \cdot t_A) \\ x_{O_i}^{t_B} = v_w \cdot t_B + A \cdot \sin(\omega_f \cdot t_B) \end{cases} \tag{3}$$

Then, the line l_{BOi} can be given as

$$l_{BO_i} : y_{t_B} = \left(x_{t_B} - x_{O_i}^{t_B}\right) \tan(\omega_s \cdot t_B) \tag{4}$$

The trajectory of the $(i + 1)$th abrasive in UAMEG can be expressed by

$$\begin{cases} x_{i+1} = v_w t + r\cos(\omega_s(t - (i+1)\Delta_t)) + A\sin(\omega_f t) \\ y_{i+1} = r\sin(\omega_s(t - (i+1)\Delta_t)) \end{cases} \quad (i = 0, 1, 2...), \tag{5}$$

where ω_f ($\omega_f = 2\pi f$) is the angular frequency of ultrasonic vibration.

For the point A (x_{tA}, y_{tA}) is the intersection of the trajectory of the $(i + 1)$th abrasive and the extension line of l_{BOi}, the following simultaneous equations system can be derived:

$$\begin{cases} x_{t_A} &= v_w \cdot t_A + r \cdot \cos(\omega_s \cdot (t_A - \Delta_t)) + A \cdot \sin(\omega_f \cdot t_A) \\ y_{t_A} &= r \cdot \sin(\omega_s \cdot (t_A - \Delta_t)) \\ y_{t_A} &= \left(x_{t_A} - x_{O_i}^{t_B}\right) \cdot \tan(\omega_s \cdot t_B) \end{cases} \tag{6}$$

From the simulation results in previous research [14], it can be seen that the instantaneous abrasive cutting thickness h repetitively oscillates as analogous sine wave at ultrasonic frequency, which indicates that intermittent cutting is achieved in UAMEG from the view of single abrasive. In every ultrasonic period, when cutting abrasive withdraws from unmachined material, instantaneous abrasive cutting thickness keeps zero. The instantaneous abrasive cutting thickness increases from zero when the cutting abrasive cuts into unmachined material to a maximum value. Subsequently, it decreases to zero at the point the cutting abrasive withdraws from unmachined material.

In micro-machining, machining mechanism is colossal influenced by the ratio of effective tool cutting edge radius to undeformed chip thickness. For abrasive edge radius tends to the same scale with the undeformed chip thickness, a small fluctuation of undeformed chip thickness significantly influences the grinding process [6]. Considering abrasive cutting edge radius, undeformed chip thickness in micro-end grinding is proportional to instantaneous abrasive cutting thickness, abrasive radius, height of protrusion of abrasives, and cutting depth, as shown in Fig. 3.

According to indentation test [21, 22], fracture crack initiation and growing process can be demonstrated as follows:

a. As the indenter tip penetrates into the surface of the sample of brittle material under small load, the material exhibits elasticity with formation of plastically deformed zone in the form of a hemispheric enclave. The bottom of this plastic zone is conserved under high residual stresses.
b. With the increase of the load, a crack called median crack is initiated from the bottom of plastic zone along the axial direction of the load.
c. During unloading half cycle, the lateral crack is initiated, oriented in the lateral direction to the load axis.
d. As unloading continues, lateral crack grows toward the surface.

Considering analogous sine-waved instantaneous abrasive cutting thickness, and analogizing crack theory above to micro-grinding process, crack initiation and growing process

Fig. 3 Abrasive cutting process under intermittent machining in UAMEG

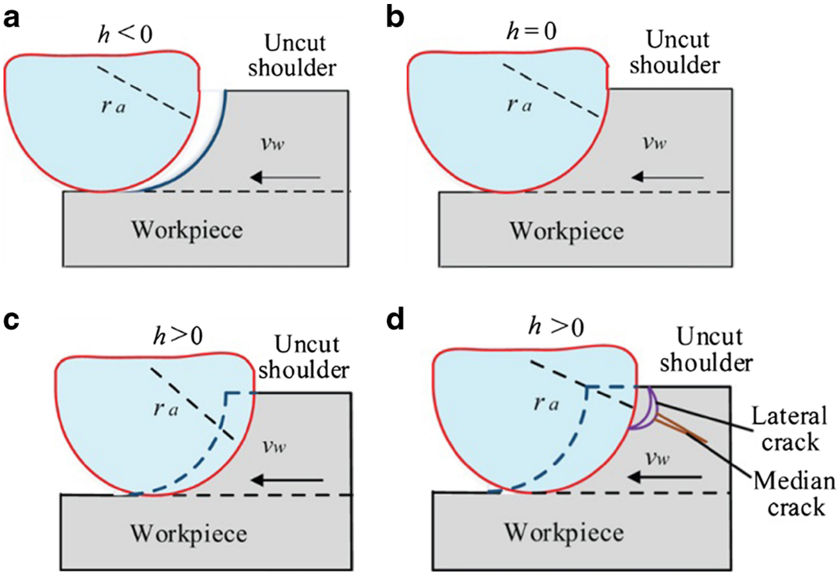

during abrasive-workpiece interaction in UAMEG can be demonstrated as shown in Fig. 3. When h is zero, the abrasive withdraws from the uncut shoulder and only slides on the machined surface. As h increases the abrasive cuts gradually into uncut shoulder material, the material exhibits elasticity followed by formation of plastically deformed zone in the form of a hemispheric enclave. When the maximum undeformed chip thickness ($t_{\max}$) exceeds the critical undeformed chip thickness (below which chips will not form), chips are formed via plastic deformation. At some h values, where $t_{\max}$ and cutting force are in excess of the critical values of ductile-brittle transition, median cracks initiate. Then, median cracks grow with h increasing. As the abrasive passed, which is analogous to the unloading half cycle, the residual stresses beneath the plastic zone propagate lateral cracks. Then, the lateral cracks grow toward surface of uncut shoulder, and thus, a part of uncut shoulder material is to be removed via brittle pattern.

There exist three critical values of instantaneous abrasive cutting thickness.

From Fig. 4, the maximum undeformed chip thickness $t_{\max}$ can be expressed as

$$t_{\max} = r_a - \left(r_a^2 + h^2 - 2 \cdot r_a \cdot h \cdot \sin\theta_{\max}\right) \tag{7}$$

$$\cos\theta_{\max} = \frac{r_a - a_p}{r_a} \tag{8}$$

Here, h_{c2} is defined as the critical value of instantaneous abrasive cutting thickness for median crack initiation, where

Fig. 4 Geometry of critical condition of ductile machining

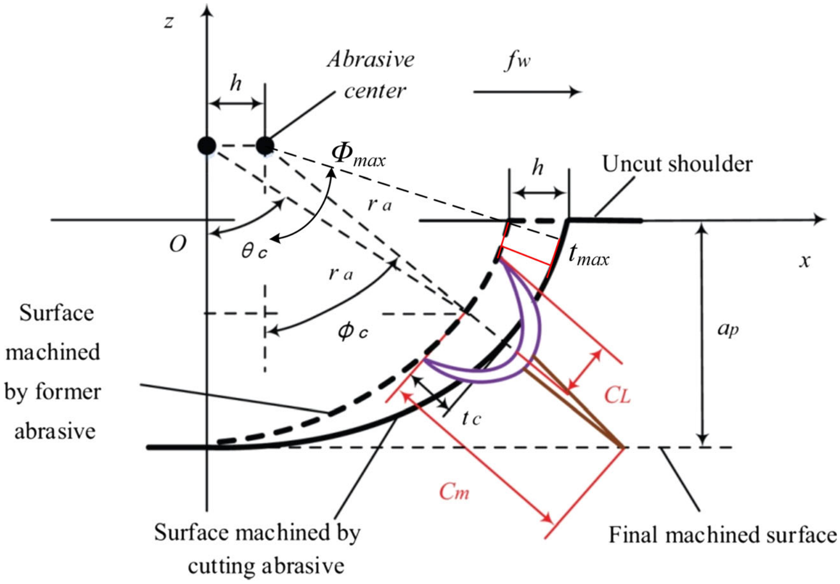

the maximum undeformed chip thickness $t_{\max}$ is equal to t_c, which is the critical undeformed chip thickness for ductile brittle transition. Then, h_{c2} can be expressed as

$$t_{\mathrm{c}} = r_a - \left(r_a^2 + h_{c2}{}^2 - 2\cdot r_a\cdot h_{c2}\cdot\sin\theta_{\max}\right) \tag{9}$$

When $t_{\max}$ is less than t_c, there will be no fracture crack initiation. In this case, material elastic flow and sharing formation are the predominant material removal mode. When $t_{\max}$ is larger than t_c, median crack initiates in the orientation between which the included angle is $\Phi_{\max}$.

There exists a critical condition of ductile region grinding, as shown in Fig. 4, where the median cracks and lateral cracks can exactly get clear of the final machined surface. At this condition, maximum material removal rate can be achieved under ductile region grinding.

Arif [23] demonstrates that fracture of final machined surface is predominantly influenced by the median crack. The length of median crack is equal to seven times of the radius of lateral crack [21], i.e.,

$$C_m = 7C_L \tag{10}$$

The critical condition that both of these two crack systems approach the final machined surface can be given as

$$C_m\cdot\cos\theta = C_L \tag{11}$$

$$\theta = \arccos\ \left({}^1\!/_7\right) = 81.79^\circ \tag{12}$$

As the θ range from 0 to 81.79°, depth of damage due to median crack remains more than damage depth due to radius of lateral crack. Beyond this limit of θ, C_L is too small to reach the final machined surface. Thus, if median cracks do not approach the final machined surface, ductile machining can be achieved.

From the geometry of Fig. 4, critical condition which obtains final fracture-free machined surface can be written as

$$C_m\cdot\cos\phi_c + r_a\cdot\cos\theta_c = r_a \tag{13}$$

$$(C_m - t_c)\cos\varphi_c + r_a\cos\varphi_c = r_a \tag{14}$$

$$(r_a - t_c)\cdot\cos\varphi_c = r_a\cos\theta_c \tag{15}$$

$$r_a^2 + h_{c1}{}^2 - 2\cdot r_a\cdot h_{c1}\cdot\sin\theta_{\mathrm{c}} = r_a - t_{\mathrm{c}} \tag{16}$$

where t_c is the critical undeformed chip thickness for ductile brittle transition, r_a is the radius of the abrasive, and h_{c1} is the critical instantaneous abrasive cutting thickness for ductile grinding.

From Lawn and Marshall's [22] research, the critical median crack length C_m can be expressed as

$$C_m = \mu_0\left[\frac{K_{\mathrm{IC}}^2}{H^2}\right] \tag{17}$$

where μ_0 is the geometrical constant which depends on material properties, H is the material hardness, and K_{IC} is the material static fracture toughness.

Then, substituting Eqs. (13) and (14) into Eq. (15), h_{c1} can be expressed as

$$h_{c1} = r_a\cdot\sin\theta_c - \sqrt{r_a^2\cdot\left(\sin^2\theta_c - 1\right) + \left(\frac{\cos\theta_c\cdot C_m}{1-\cos\theta_c}\right)^2} \tag{18}$$

It can be seen from Eq. (14) that the critical median crack length C_m leads to a limit to the critical instantaneous abrasive cutting thickness h_{c1} under given abrasive radius r_a and cutting speed. This defines the upper limit of material removal rate for ductile machining. Critical instantaneous abrasive cutting thickness increases with the decrease of critical median crack length. That means lower critical median crack length improves material removal rate under ductile machining.

Malekian [25] researches the minimum uncut chip thickness in micro-machining. The presence of a critical or minimum uncut chip thickness is observed when the machining operations are performed using a tool with a finite edge radius. A stagnation point, which happens at a critical or stagnant angle, θ_m, determines the value of the minimum uncut chip thickness, namely,

$$h_m = r_a(1 - \cos\theta_m) \tag{19}$$

Both minimum energy approach and infinite shear strain approach are adopted to model the minimum uncut chip thickness in micro-machining. Then, it came to the conclusion that

$$\theta_m = \beta_s \tag{20}$$

where β_s is the friction angle between the workpiece and the rake face during shearing and can be expressed as

$$\mu = \tan\beta_s \tag{21}$$

where μ is the friction coefficient and can be expressed as

$$\mu = A\frac{\tau}{p^{1/3}}\left(\frac{3}{4E'}\right)^{2/3} \tag{22}$$

where A is a constant determined by contact geometry; τ is the critical shear stress at the interface, which may be an oxide film; P is the normal load; and E' is the effective elastic modulus of the contact materials.

2.2 Material removal mechanism in grinding region II

As analyzed above, plowing is assumed to be the predominant mechanism of interaction between abrasives and workpiece in grinding region II. For modeling of the plowing force, it is essential that the contact geometry be established precisely. Bolshakov and Pharr [24] examined the significance of pileup for rigid conical indenters and found that if pileup is neglected, the true contact area can be underestimated by as much as 60 %. Thus, a complete understanding of pileup, as well as material springback, is crucial to establish accurately the contact geometry. The degree of pileup is a unique function of the strain-hardening exponent n, which can be conveniently described as [26, 27] (in this section, h would be instead by another letter)

$$c^2 = a_c^2/2\ Rh \tag{23}$$

where c^2 is a parameter, which has a simple physical interpretation in the limit of small penetration depths; it is the ratio of the depth along which contact is made to the total depth of penetration, and $c^2 > 1$ implies that material piles up. From Norbury and Samuel's experimental data [28], pileup is represented by the normalized pileup parameter s_p/h, where $s_p/h = c^2 - 1$. Then, the empirical relation between s/h and n can be expressed as

$$\frac{s_p}{h} = \frac{1}{2}\left(\frac{2+n}{2}\right)^{2(1-n)/n} - 1 \tag{24}$$

In micro-hardness tests, the elastic recovery would occur in the vicinity of remaining indentation impression after the indenter is removed so that the indentation size would shorten to a certain degree [29]. Analogizing this phenomenon to abrasive scratching process, elastic recovery of the part of material that impressed by abrasive tip but cannot be removed by chip formation would lead to a certain contact area between flank surface of the tip, as shown in Fig. 5. As demonstrated by Gauthier [30] in the research of elastic recovery of a scratch in polymethylmethacrylate surface, the elastically recoverable height s_e can be expressed as

$$s_e = \sqrt{\frac{2c}{\tan\theta}\frac{\sigma_{\text{yield}}}{E^*}a_f} \tag{25}$$

where a_f is the plastic contact radius, c is the ratio of "hardness" to yield stress, θ is the half apex angle of a conical tip, and σ_{yield} is the yield stress.

Material springback was investigated in Arcona's [31] research on tool force model for precision machining. An empirical model of material springback was developed to describe this phenomenon, in which the height of springback was demonstrated to be of linear relationship with tool edge radius and the ratio of material hardness to elastic modulus.

$$s_e = k_1 r \frac{H}{E} \tag{26}$$

Under the plowing effect of abrasives arrayed in inner region of wheel end face, micro-cambered groove arrays are left over as remnant in grinding region II.

2.3 Material removal mechanism in grinding region III

In grinding region III, sliding occupies the absolute influence on mechanism of interaction between abrasives and workpiece, as shown in Fig. 6. Unlike in grinding region II, there exists no pileup phenomenon in front of tool tip above minimum uncut chip thickness. Material encountering the abrasive rack face is impressed and flows beneath the abrasive. Then, material flows along the undersurface of tool tip and then rebounds to the original height after the abrasive passes.

Because direction of main cutting speed of most abrasives in grinding region III is approximately perpendicular to flank of cambered grooves in grinding region II, surface with grooves can be effectively smoothed due to material elastic deformation caused by sliding effect. Moreover, if material is removed in the way of fracture crack and the cracks extend into machined surface in grinding region I, the remained cracks cannot be removed in sliding process.

3 Force modeling of single abrasive

3.1 Individual abrasive force modeling in grinding region I

3.1.1 Below the minimum undeformed chip thickness

In micro-grinding process, the material below the minimum undeformed chip thickness is plastically deformed under the press of abrasive without chip formation, which is defined as plowing effect. This plastic deformation is similar to the

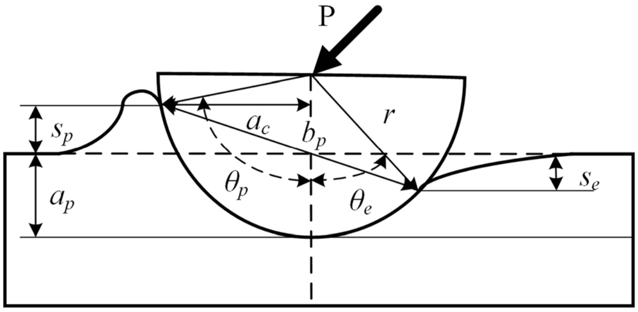

Fig. 5 Abrasive-material plowing effect

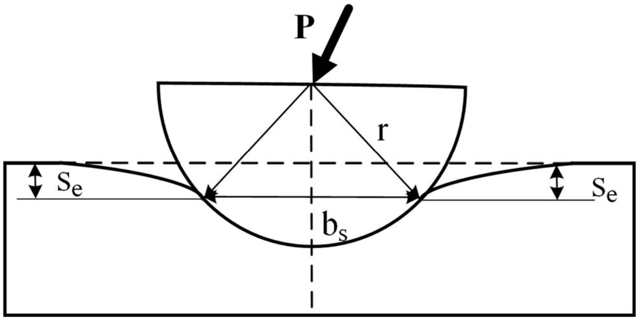

Fig. 6 Abrasive-material sliding effect

material deformation in spherical indentation process. Brinell indentation hardness test was adopted to describe the single abrasive interaction process (Fig. 7), for the material behavior beneath a Brinell ball resembles the material deformation below an abrasive. The Brinell hardness number (HB) is defined as the ratio of load (F_{Brinell}) to the curved area of indentation as follows:

$$\mathrm{HB} = \frac{2F_{\mathrm{Brinell}}}{\pi D\left(D - \sqrt{D^2 - b^2}\right)} \tag{27}$$

where D is the ball diameter and b is the impression diameter.

Then, the stress in plowing region can be associated with Brinell hardness test. Considering the minimum undeformed chip thickness and material springback, the central angle θ_1 corresponding to material springback can be expressed as

$$\cos\theta_1 = \frac{r - s_e}{r} \tag{28}$$

Then, the including angle of plowing loading direction and vertical can be expressed as

$$\alpha_p = \frac{\theta_m - \theta_1}{2} \tag{29}$$

Then, the real impression diameter of plowing effect b_p in UAMEG can be deduced as

$$b_p^{'} = 2r\sin\alpha_p \tag{30}$$

$$b_p = b_p^{'}\sin\eta_h \tag{31}$$

Then, the load F_{dp} that acts vertically to the plowing-interacting surface between abrasive and workpiece due to plowing effect in ductile removal can be expressed as

$$F_{dp,1} = \mathrm{HB}\pi\mathrm{r}\left(2r - \sqrt{(2r)^2 - b_p^2}\right) \tag{32}$$

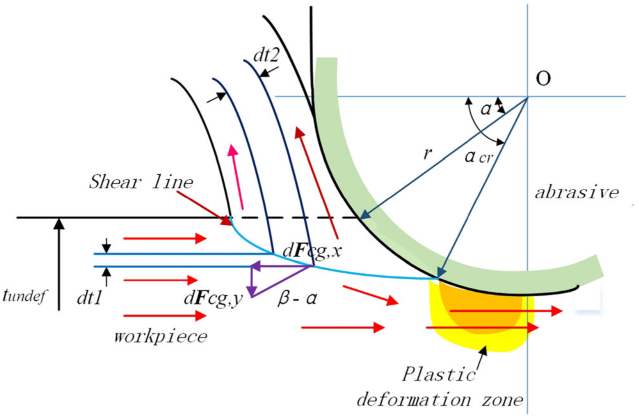

Fig. 7 Geometrical schematic of single abrasive material in the main grinding zone

In addition, friction is generated between the abrasive and the workpiece due to relative movement. The circumferential force, normal force, and radial force can be estimated by combining the indentation effect with the friction as

$$F_{c,gp1} = F_{dp}\left(\sin_{\alpha_p}\sin\frac{\eta_h}{2} + \mu\cos\alpha_p\cos\frac{\eta_h}{2}\right) \tag{33}$$

$$F_{n,gp1} = F_{dp}\left(\cos\alpha_p - \mu\sin\alpha_p\right) \tag{34}$$

$$F_{r,gp1} = F_{dp}\left(\sin_{\alpha_p}\cos\frac{\eta_h}{2} - \mu\cos\alpha_p\sin\frac{\eta_h}{2}\right) \tag{35}$$

3.1.2 Above the minimum undeformed chip thickness

In micro-grinding of hard and brittle materials, material is removed in the way of chip formation due to plastic deformation, when the maximum undeformed chip thickness is below the critical undeformed chip thickness of crack initiation and above the minimum undeformed chip thickness. Then, the micro-cutting mechanism can be represented by applying Merchant's model to each of the infinitesimal undeformed chip thickness elements [32, 33]. Considering a single element of undeformed chip thickness, dt_i, corresponding to the associated local friction angle, local rake angle, and local contact angle in feed direction, the incremental circumferential force, normal force, and radial force per unit undeformed chip thickness element due to chip formation in the three-dimensional simplified configuration can be expressed as

$$dF_{c,gc1} = \frac{\tau_s\cos(\beta_i - \alpha_i)}{\cos(\varphi_i + \beta_i - \alpha_i)}\cos\eta_{h,i} \tag{36}$$

$$dF_{n,gc1} = \frac{\tau_s\sin(\beta_i - \alpha_i)}{\cos(\varphi_i + \beta_i - \alpha_i)} \tag{37}$$

$$dF_{r,gc1} = \frac{\tau_s\cos(\beta_i - \alpha_i)}{\cos(\varphi_i + \beta_i - \alpha_i)}\sin\eta_{h,i} \tag{38}$$

where τ_s is the shear strength of the material, β_i is the local friction angle, α_i is the local rake angle, η_i is the local contact angle in feed direction, and φ_i is the local shear angle. As shown in Fig. 8, η_i has a relationship with the instantaneous abrasive cutting thickness, which can be expressed as

$$\eta_h = \cos^{-1}\left(\frac{R_g - h}{R_g}\right) \tag{39}$$

The effective rake angle α_s is negative when the undeformed chip thickness is less than the abrasive radius, which can be expressed as follows according to geometrical relationship of Fig. 7:

$$\alpha_s = \sin^{-1}\frac{r - a_p}{r} \tag{40}$$

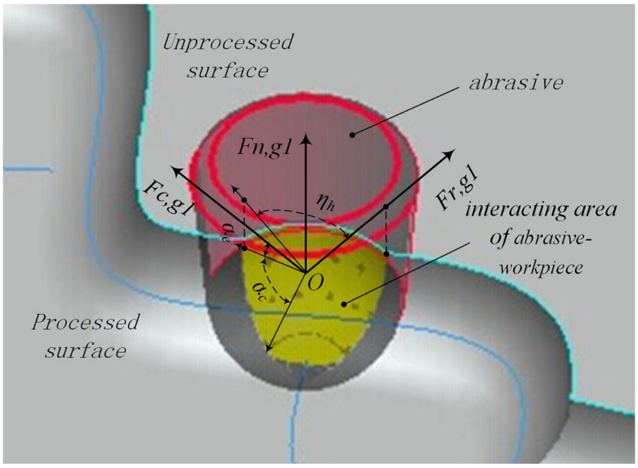

Fig. 8 Schematic of single abrasive material in the main grinding zone

The critical rake angle α_c corresponding to the minimum undeformed chip thickness can be expressed as

$$\alpha_c = \frac{\pi}{2} - \theta_m \tag{41}$$

In UAMEG, the interacting area between the hemispherical abrasive and workpiece changes with the fluctuation of the instantaneous abrasive cutting thickness in sine wave. The instantaneous chip formation force can be obtained by means of double integral of incremental force per unit undeformed chip thickness element over the interacting area. Then, the overall circumferential force, normal force, and radial force due to chip formation for individual abrasive can be expressed as

$$F_{c,gc1} = \int_{\alpha_c}^{\alpha_e} \int_0^{\eta_h} \frac{\tau_s \cos(\beta_i - \alpha_i)}{\cos(\varphi_i + \beta_i - \alpha_i)} \cos\eta_i d\eta_i d\alpha_i \tag{42}$$

$$F_{n,gc1} = \int_{\alpha_c}^{\alpha_e} \int_0^{\eta_h} \frac{\tau_s \sin(\beta_i - \alpha_i)}{\cos(\varphi_i + \beta_i - \alpha_i)} d\eta_i d\alpha_i \tag{43}$$

$$F_{r,gc1} = \int_{\alpha_c}^{\alpha_e} \int_0^{\eta_h} \frac{\tau_s \cos(\beta_i - \alpha_i)}{\cos(\varphi_i + \beta_i - \alpha_i)} \sin\eta_i d\eta_i d\alpha_i \tag{44}$$

3.1.3 Above the critical undeformed chip thickness of crack initiation

When the maximum instantaneous abrasive cutting thickness exceeds the critical value of crack initiation, material removal mechanism will be partially changed to be fracture crack. Thus, grinding forces should be predicted in the homologous way, namely, grinding force modeling for brittle region removal. As analyzed above, crack, as well as indentation loading, will grow with increasing of instantaneous abrasive cutting thickness under brittle-region removal. Final surface without crack remnants is desired in processing of hard and brittle materials. Thus, modeling of grinding forces under brittle region removal is conducted below the critical condition of ductile region grinding given above for force prediction margin, at which the maximum fracture force of ductile region grinding is approached. In this case, from spherical indentation research, normal load between abrasive and workpiece in brittle removal at median crack length of C_m can be expressed as

$$F_{b,C_m}{}^{4/3} = C_m^{2/3} (4\pi/r)^{2/3} \chi^{-1} \left(K_c E^{-1/2} H^{5/6} \right) \tag{45}$$

Then, considering friction effects in interacting surface of abrasive and material, the circumferential force, normal force, and radial force for individual abrasive grinding under brittle removal can be expressed as

$$F_{c,gb1} = F_{b,C_m} \left(\sin\varphi_c \sin\frac{\eta_h}{2} + \mu\cos\varphi_c \right) \tag{46}$$

$$F_{n,gb1} = F_{b,C_m} (\cos\varphi_c - \mu\sin\varphi_c) \tag{47}$$

$$F_{r,gb1} = F_{b,C_m} \left(\sin\varphi_c \cos\frac{\eta_h}{2} - \mu\cos\varphi_c \sin\frac{\eta_h}{2} \right) \tag{48}$$

3.2 Individual abrasive force modeling in grinding region II

As demonstrated above, plowing effects is the predominant mechanism of interaction between abrasives and workpiece in grinding region II. However, according to the research results of the spherical indentation process, material pileup should be taken into account for force modeling to consider the plowing effects. After initially sinking-in at small depth, the pileup evolves and increases gradually as the indenter is driven into the material, which can significantly affect the contact area of interaction. The geometrical schematic of contact area in this grinding region is shown in Fig. 5. Scratching depth a_p in grinding region II is assumed to be equal to the minimum uncut chip thickness h_m for all the plowing abrasives for simplification. Then, maximum rake angle and maximum relief angle can be given as

$$\cos\alpha_{p,2} = 1 - \frac{s_{p,2} + a_{p,2}}{r} \tag{49}$$

$$\cos\beta_{p,2} = 1 - \frac{s_{e,2}}{r} \tag{50}$$

Then, the diameter of the contact area can be expressed as

$$b_{p,2} = 2r\sin\left(\frac{\alpha_{p,2} + \beta_{p,2}}{2} \right) \tag{51}$$

The load F_{dp} that acts vertically to the plowing-interacting surface between abrasive and workpiece can be expressed as

$$F_{p,2} = \mathrm{HB}\pi\mathrm{r}\left(2r - \sqrt{(2r)^2 - b_{p,2}^2}\right) \tag{52}$$

In this grinding region, it is assumed that the abrasive tip completely sinks into the workpiece material in the radial direction. The circumferential force, normal force, and radial force of individual abrasive can be estimated by combining the indentation effect with the friction as

$$F_{c,gp2} = F_{p,2}\left(\sin_{\alpha_{p,2}} + \mu\cos\alpha_{p,2}\right) \tag{53}$$

$$F_{n,gp2} = F_{p,2}\left(\cos\alpha_{p,2} - \mu\sin\alpha_{p,2}\right) \tag{54}$$

$$F_{r,gp2} = 0 \tag{55}$$

3.3 Individual abrasive force modeling in grinding region III

As investigated above, it is assumed that there exists no pileup phenomenon in front of tool tip in grinding region III. But, the material springback should be considered for sliding force modeling. As shown in Fig. 6, the contact diameter can be given as

$$b_{s,3} = 2\sqrt{r^2 - (r - s_e)^2} \tag{56}$$

Since the axis of sliding-interacting surface is vertically to the workpiece surface, the normal grinding force of individual abrasive is equal to the load F_{dp} acting vertically to the sliding-interacting surface, which can be expressed as

$$F_{n,g,s,3} = F_{s,3} = \mathrm{HB}\pi\mathrm{r}\left(2r - \sqrt{(2r)^2 - b_{s,3}^2}\right) \tag{57}$$

The circumferential force of individual abrasive can be estimated by combining the indentation effect with the friction as

$$F_{c,g,s,3} = \mu F_{s,3} \tag{58}$$

The radial force of individual abrasive can be expressed as

$$F_{r,g,s,3} = 0 \tag{59}$$

In this section, the models of circumferential force, normal force, and radial force of individual abrasive are developed, respectively, for these three grinding regions defined above, considering material brittle fracture, plowing effect, and sliding effect.

3.4 Force modeling considering the size effect

UAMEG belongs to the micro-machining. Size effect is the most essential difference between micro-machining and conventional machining. So, the influence of size effect should be considered in the force modeling of UAMEG. As demonstrated above, various theories with respect to the mechanism of size effect have been proposed, such as the intensified influence of plowing force in micro-cutting, material-strengthening effect due to the decrease of dislocation density, weakening of material-softening effect due to the decrease of cutting temperature, material strain rate increasing, the enhancement of strain gradient effect, and the influence of material surface energy consumption.

An individual abrasive force model is developed above considering the size effect from the point of the influence of plowing force and sliding force. According to the influence mechanism of the plowing force in this section, material-strengthening effect due to the decrease of dislocation density into individual abrasive force modeling to further take account of the size effect.

To characterize the material-strengthening effect in micro-scale material cutting, Lai et al. [34] improved the J-C material constitutive model based on the strain gradient plasticity theory. J-C constitutive model is widely used in the situation of large-strain gradient, strain rate, and temperature, which characterize the material flow stress. It can be given as follows:

$$\sigma_{\mathrm{JC}} = \left[A + B(\varepsilon)^n\right]\left[1 + C\ln\left(\frac{\dot{\varepsilon}}{\dot{\varepsilon}_0}\right)\right]\left[1 - \left(\frac{T - T_0}{T_{\mathrm{melt}} - T_0}\right)^m\right] \tag{60}$$

where σ_{JC} is the plastic equivalent stress; ε is the equivalent strain; ε is the equivalent strain rate; ε is the reference strain rate; T_{melt} is the melting temperature of the workpiece material; T_0 is the phase-transition temperature of the workpiece material; and A, B, C, m, and n are the constants.

The above equation indicates that material flow stress has nothing to do with cutting scale in the J-C model. So, to characterize the size effect, scale variable I is introduced to consider the change of cutting dimension. The improved J-C model can be expressed as

$$\sigma = f(\sigma_{\mathrm{conv}}, l) \tag{61}$$

where σ_{conv} is equal to σ_{JC}, in macro-scale cutting, $\sigma = \sigma_{\mathrm{JC}}$.

According to Taylor dislocation model and strain gradient plasticity theory, material plastic flow stress can be expressed as the function of dislocation density, which can be given as

$$\sigma = 3\alpha \mathrm{Gb}\sqrt{\rho} = 3\alpha \mathrm{Gb}\sqrt{\rho_s + \rho_g} \tag{62}$$

where α is the rake angle, G is the shear modulus (MPa), b is the Burgess vector (nm), ρ is the dislocation density of workpiece materials, ρ_g is the geometrically necessary dislocation density, and ρ_s is the statistical storage dislocation density, which is measured by experiment under no strain gradient. The relationship between traditional plastic flow stress and statistical storage dislocation density is expressed as

$$\sigma_{\mathrm{conv}} = 3\alpha \mathrm{Gb}\sqrt{\rho_s} \tag{63}$$

To assess the total dislocation density, the coefficient μ is introduced (according to the research of the Lai [34], the value of μ is 0.38). Then, the plastic flow stress can be expressed as

$$\sigma \;=\; 3\alpha \mathrm{Gb}\sqrt{\rho_s^{\mu} + \rho_g^{\mu}} \tag{64}$$

By substituting Eqs. (63) and (64) to Eq. (62), σ can be rewritten as

$$\sigma \;=\; \sigma_{\mathrm{conv}}\sqrt{1 + \left(\frac{\rho_g}{\rho_s}\right)^{\mu}} \tag{65}$$

Geometrically, necessary dislocation density can be expressed as

$$\rho_g = \frac{2\eta}{b} \tag{66}$$

where η is the strain gradient.

Then, the material constitutive equation considering statistical storage dislocation density and geometrically necessary dislocation density can be expressed as

$$\sigma \;=\; \sigma_{\mathrm{conv}}\sqrt{1 + \left(\frac{18\alpha^2 G^2 b\eta}{\sigma_{\mathrm{conv}}^2}\right)^{\mu}} \tag{67}$$

The traditional plastic flow stress can be represented by the conventional J-C constitutive model. Then, the material constitutive equation considering the statistical storage dislocation density and geometrically necessary dislocation density can be expressed as

$$\sigma = \sigma_{J-C}\sqrt{1 + \left(\frac{18\alpha^2 G^2 b\eta}{\sigma_{J-C}^2}\right)^{\mu}} \tag{68}$$

According to MelKote's [35] research, strain gradient can be obtained through the first deformation zone as follows

$$\eta = \frac{1}{L} \tag{69}$$

where L is the length of first deformation zone.

Substituting Eq. (69) to Eq. (68), the material constitutive equation can be expressed as

$$\sigma = \sigma_{J-C}\sqrt{1 + \left(\frac{18\alpha^2 G^2 b}{\sigma_{J-C}^2 L}\right)^{\mu}} \tag{70}$$

Minimum undeformed chip thickness has a great effect in micro-scale cutting, especially when the undeformed chip thickness has the same level with micro-cutting edge. So, the first deformation zone length L can be solved in two cases, with and without chip formation. Kim et al. [36] conducted the MD simulation of this phenomenon, as shown in Fig. 9; when $h \geqq h_{\min}$, the first deformation zone length L can be expressed as

$$L = \frac{h}{\sin(\phi)} \tag{71}$$

$$\phi = \frac{r\cos\alpha_n}{1 - r\sin\alpha_n} \tag{72}$$

$$r = \frac{h_{\min}}{h} \tag{73}$$

where h is the undeformed chip thickness, $h_{\min}$ is the minimum undeformed chip thickness, and φ is the shearing angle.

As shown in Fig. 9b, when $h < h_{\min}$, Eqs. (71)–(73) are not suitable to calculate L, because the shearing angle and the chip thickness t can be seen as zero. Contact arc length between tool nose and workpiece can be regarded as the length of first deformation zone. So, the first deformation zone length L can be expressed as

$$L = \frac{\arccos\left(\frac{R-h}{R}\right)\pi \mathrm{R}}{180} \tag{74}$$

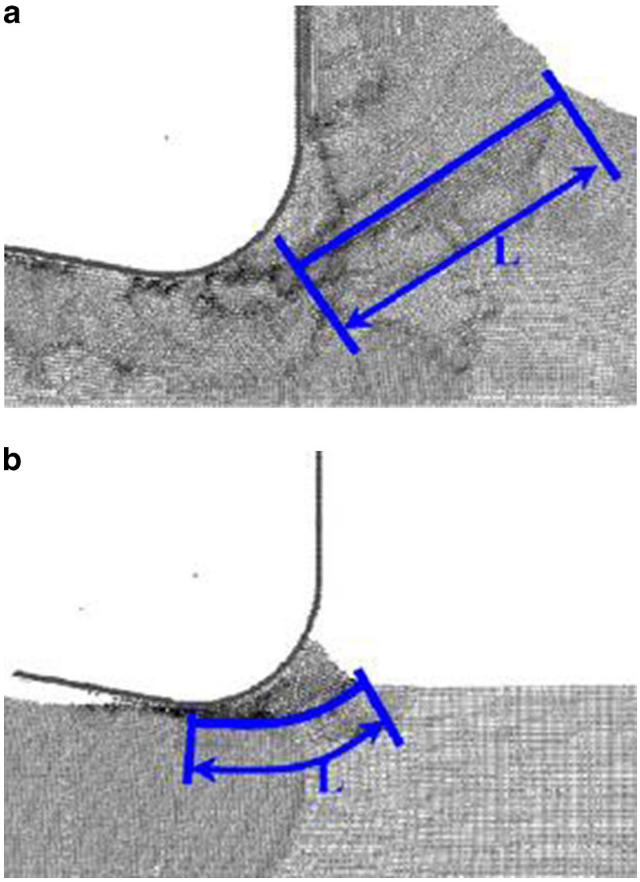

Fig. 9 Schematic diagram of machining region considering the tool edge radius. **a** With chip formation and **b** without chip formation

In conclusion, the material constitutive model considering the size effect of micro-cutting scale can be expressed as follows

$$\sigma = \sigma\left(\varepsilon, \varepsilon, T, \dot{L}, h_{\min}\right) = \sigma_{J\text{-}C}\sqrt{1 + \left(\frac{18\alpha^2 G^2 b}{\sigma_{J\text{-}C}^2 L}\right)^{\mu}} \quad (75)$$

$$\sigma_{\mathrm{JC}} = \left[A + B(\varepsilon)^n\right]\left[1 + C\ln\left(\frac{\dot{\varepsilon}}{\dot{\varepsilon}_0}\right)\right]\left[1 - \left(\frac{T - T_0}{T_{\mathrm{melt}} - T_0}\right)^m\right] \quad (76)$$

The Oxley model [37] is adopted to calculate strain and strain rate, which is given as

$$\varepsilon = \frac{1}{2\sqrt{3}}\frac{\cos\alpha_n}{\cos(\varphi - \alpha_n)\sin\phi} \quad (77)$$

where α_n is the nominal rake angle.

Strain rate model is as follows:

$$\dot{\varepsilon} = \frac{C_{\mathrm{Oxley}}}{\sqrt{3}}\frac{Vg\cos\alpha_n}{\cos(\phi + \alpha_n)}\frac{\sin\phi}{t_0 - t_m} \quad (78)$$

where C_{Oxley} is the constant, v_g is the abrasive speed, t_o is the undeformed chip thickness, t_m is the minimum undeformed chip thickness, and α_n is considered to be equal to the equivalent plow rake angle α_p.

For convenience, the undeformed chip thickness in material constitutive model above is characterized by individual abrasive instantaneous chip thickness in the UAMEG. Due to the influence of ultrasonic vibration, when the interrupted cutting is realized, individual abrasive instantaneous chip thickness various in a high frequency and the average chip thickness decreases dramatically. The plastic flow stress is inversely proportional to undeformed chip thickness in the above material constitutive model. Therefore, with the abrasive chip thickness decreasing in UAMEG, material plastic flow stress will increase because of the size effect.

3.5 Modeling of overall grinding force of the wheel

3.5.1 Effective cutting ages on micro-grinding wheel end face

Randomness of the size and distribution of abrasives on grinding wheel should be considered for development of overall grinding force on the whole wheel end face. In cylindrical grinding, the effective cutting edge number of grinding zone is connected with grinding parameters. Dynamic effective cutting edge number is a function of static cutting edge density and grinding parameters. In face grinding, effective cutting edge number is irrelevant to grinding parameters in plowing and sliding zone, except in the main grinding zone. But, the abrasives in the main grinding zone account for a small percentage in the total abrasives of whole wheel end face. For convenience, the influence of grinding parameters on effective cutting edge number in the main grinding zone is ignored in this paper. Then, the effective cutting edge number is considered to be approximately equal to wheel static cutting edge density, namely,

$$C_d = C_s \quad (79)$$

The static cutting edge density model presented by Hacker [38] is adopted in this work, which is given as follows:

$$C_s = A_s Z^{k_s} \quad (80)$$

where C_s is the static cutting edge density; A_s and k_s are the constants, which can be determined via grinding experiments; and z is the grinding depth.

The topography of micro-grinding wheel plays a crucial role in modeling of the micro-grinding process with high reliability. In Park's [30] research of the wheel surface micro-structure, the values of A_s and k_s for fresh tool and worn tool are obtained. In this work, the average values of A_s and k_s of fresh tool and worn tool are adopted to calculate the expected value of chip thickness. The average values of A_s and k_s are, respectively, 2.283 and 0.88735.

3.5.2 Grinding force modeling of grinding region 1

Below the minimum instantaneous abrasive cutting thickness In the case of the cutting thickness below the minimum instantaneous abrasive cutting thickness, plowing effect plays a major role in the interaction between the abrasive and workpiece materials. The abrasive in the main grinding at the x axis is defined as the i_{th} abrasive. The tangential force, normal force, and radial force of the i_{th} abrasive are defined as $F_{ci,p1}$, $F_{ni,p1}$, and $F_{ri,p1}$, respectively. Then, the component force along the normal direction, x axis, and y axis of the total grinding force in the main grinding zone can be expressed as

$$F_{n,p1} = \sum_{i=1}^{n_1} F_{ni,gp1} \tag{81}$$

$$F_{x,p1} = \sum_{i=1}^{n_1} F_{ri,gp1} \cos\theta_{i,1} \tag{82}$$

$$F_{y,p1} = \sum_{i=1}^{n_1} F_{ci,gp1} \sin\theta_{i,1} \tag{83}$$

where $F_{n,p1}$, $F_{x,p1}$, and $F_{y,p1}$ are the component forces along the normal direction, x axis, and y axis, respectively; n_1 is the cutting edge number of the main grinding zone; and $\theta_{i,1}$ is the rotation angle of the i_{th} abrasive in main grinding zone.

The solution of n_1 and $\theta_{i,1}$ can be given as

$$n_1 = C_s(2\pi r_s)\sqrt{b^2-4ac} \tag{84}$$

$$\theta_{i,1} = \frac{\pi}{2n_1} i \ , \qquad\qquad i = 1, 2 \cdots n_1 \tag{85}$$

Above the minimum instantaneous abrasive cutting thickness Based on the plastic shear theory, when the chip thickness is above the minimum undeformed chip thickness, shearing effect contributes mainly to the grinding force between the abrasive and workpiece. The tangential force, normal force, and radial force of the i_{th} abrasive are defined as $F_{ci,c1}$, $F_{ni,c1}$, and $F_{ri,c1}$, respectively. Then, the component force along the normal direction, x axis, and y axis of the total grinding force in the main grinding zone can be expressed as

$$F_{n,c1} = \sum_{i=1}^{n_1} F_{ni,gc1} \tag{86}$$

$$F_{x,c1} = \sum_{i=1}^{n_1} F_{ri,gc1} \cos\theta_{i,1} \tag{87}$$

$$F_{y,c1} = \sum_{i=1}^{n_1} F_{ci,gc1} \sin\theta_{i,1} \tag{88}$$

where $F_{n,c1}$, $F_{x,c1}$, and $F_{y,c1}$ are the component forces along the normal direction, x axis, and y axis, respectively; n_1 is the cutting edge number of the main grinding zone; and $\theta_{i,1}$ is the rotation angle of the i_{th} abrasive in main grinding zone. The solutions of n_1 and $\theta_{i,1}$ are similar to Eqs. (84) and (85).

Above the critical instantaneous abrasive cutting thickness of crack initiation When the maximum instantaneous abrasive cutting thickness is above the critical value of crack initiation, the grinding force between the abrasive and workpiece is generated mainly due to brittle fracture. The tangential force, normal force, and radial force of the i_{th} abrasive are defined as $F_{ci,b1}$, $F_{ni,b1}$, and $F_{ri,b1}$, respectively. Then, the component force along the normal direction, x axis, and y axis of the total grinding force in the main grinding zone can be expressed as

$$F_{n,b1} = \sum_{i=1}^{n_1} F_{ni,gb1} \tag{89}$$

$$F_{x,b1} = \sum_{i=1}^{n_1} F_{ri,gb1} \cos\theta_{i,1} \tag{90}$$

$$F_{y,b1} = \sum_{i=1}^{n_1} F_{ci,gb1} \sin\theta_{i,1} \tag{91}$$

where $F_{n,b1}$, $F_{x,b1}$, and $F_{y,b1}$ are the component forces along the normal direction, x axis, and y axis, respectively; n_1 is the cutting edge number of the main grinding zone; and $\theta_{i,1}$ is the rotation angle of the i_{th} abrasive in main grinding zone. The solutions of n_1 and $\theta_{i,1}$ are similar to Eqs. (84) and (85).

3.5.3 Grinding force modeling of grinding region 2

Plowing effect plays a major role in the interaction between the abrasives and workpiece in grinding region 2. It is assumed in this work that the plowing effect leads to only plastic deformation of materials rather than chip formation. The proportion relationship between plowing zone area and sliding zone area is varied with the change of grinding parameters and ultrasonic vibration parameters. The boundary between plowing zone and sliding zone also varies accordingly. For convenience, this boundary is assumed to be a straight line and one of the chords of wheel circumference, which is defined as the dividing line between grinding region 2 and grinding region 3, as shown in Fig. 10.

The process of total force modeling of grinding region 2 can be illustrated as follows: firstly, all the abrasives in grinding region 2 are considered to be evenly spaced and distributed around the circumferences according to equally spaced radius. Secondly, the component force along the normal direction, x axis, and y axis of the resultant force of single abrasive forces of the abrasives distributed on every circumference are calculated using the method of discrete numerical quadrature. Finally, the three component forces of total grinding force of grinding region 2 are obtained by discrete integral of the calculated results of all abrasive circumferences along the radial direction. As shown in Fig. 10, the central angle of each circumference decreases from outer to inner in grinding region 2. The outermost circumference is defined as the first circumference, and $\theta_{1,1,2}$ is defined as the rotation angle of the first abrasive in this layer, which is given as

$$\theta_{1,1,2} = \arcsin\left(\frac{r_s - L_2}{r_s}\right) \tag{92}$$

The length of the dividing line between grinding region 2 and grinding region 3 is defined as L, and the number of the abrasives distributed on along the dividing line is defined as n_L. L and n_L can be expressed as follows:

$$L = 2\left[r_s^2 - (r_s - L_2)^2\right]^{1/2} \tag{93}$$

$$n_L = C_s L = 2C_s\left[r_s^2 - (r_s - L_2)^2\right]^{1/2} \tag{94}$$

The difference between the rotation angle of the first abrasives of adjacent two layers is defined as $\triangle\theta_{1,2}$. The rotation angle of the first abrasive in the j_{th} circumference is defined as $\theta_{j,1,2}$. Then, $\triangle\theta_{1,2}$ and $\theta_{j,1,2}$ can be given as

$$\Delta\theta_{1,2} = \frac{\left(\pi/_2 - \theta_{1,1,2}\right)}{n_L} \tag{95}$$

$$\theta_{j,1,2} = \theta_{1,1,2} + (j-1)\Delta\theta_{1,2} \tag{96}$$

The arc length of the j_{th} circumference is defined as $L_{j,2}$, and its central angle is correspondingly defined as $\theta_{j,2}$. The number of abrasives in the j_{th} circumference is defined as $n_{j,2}$. Then, $L_{j,2}$, $\theta_{j,2}$, and $n_{j,2}$ can be given as

$$\theta_{j,2} = 2\left(\frac{\pi}{2} - \theta_{j,1,2}\right) \tag{97}$$

$$L_{j,2} = \theta_{j,2}\pi r_s \tag{98}$$

$$n_{j,2} = C_s L_{j,2} \tag{99}$$

The difference of the rotation angle of adjacent abrasives in the j_{th} circumference is defined as $\triangle\theta_{\text{j,2}}$. The rotation angle of the i_{th} abrasive in the j_{th} circumference is defined as $\theta_{\text{j,i,2}}$. Then, $\triangle\theta_{\text{j,2}}$ and $\theta_{\text{j,i,2}}$ can be given as

$$\Delta\theta_{j,2} = \frac{\theta_{j,2}}{n_{j,2}} \tag{100}$$

$$\theta_{j,i,2} = \theta_{j,1,2} + (i-1)\Delta\theta_{j,2}, \qquad \theta_{j,i,2} \in \left(\theta_{j,1,2}, \pi - \theta_{j,1,2}\right) \tag{101}$$

The tangential force, normal force, and radial force of the i_{th} abrasive in the j_{th} circumference are defined as $F_{ci,gp2}$, $F_{ni,gp2}$, and $F_{ri,gp2}$, respectively. Then, the component forces of total grinding force in grinding region 2 along normal direction and y axis direction can be expressed as

$$F_{n,p2} = \sum_{j=1}^{n_l}\sum_{i=1}^{n_{j,2}} F_{ni,gp2} \tag{102}$$

$$F_{y,p2} = \sum_{j=1}^{n_L}\sum_{i=1}^{n_{j,2}} F_{ci,gp2}\sin\theta_{j,i,2} \tag{103}$$

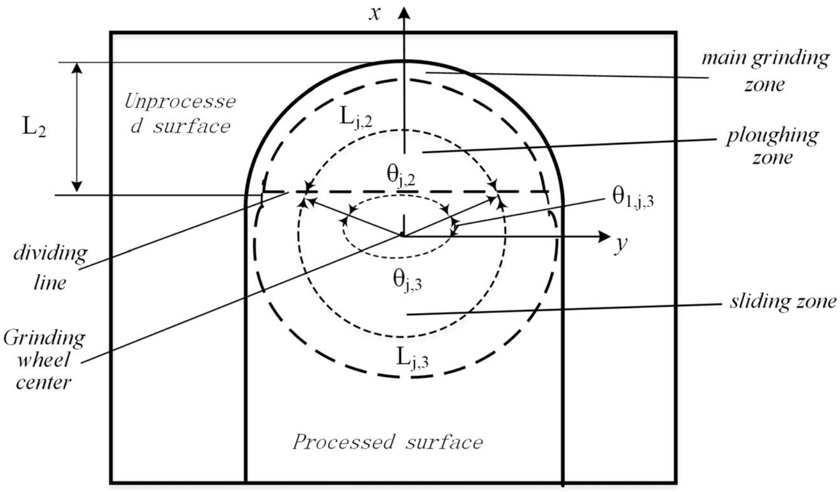

Fig. 10 Schematic diagram of grinding zone division

Due to the symmetry of grinding region 2, the resultant force in axis direction of single-grinding forces of all abrasives in this grinding region is equal to zero, namely,

$$F_{x,p2}=0 \tag{104}$$

where $F_{n,p2}$, $F_{x,p2}$, and $F_{y,p2}$ are, respectively, the component forces of total grinding force in grinding region 2 along normal direction, x axis direction, and y axis direction.

3.5.4 Grinding force modeling of grinding region 3

As mentioned above, in grinding region 3, workpiece material experiences only elastic deformation under the sliding effect, which produces pressure and friction effect between abrasives and workpiece. The proportion of sliding zone area is also influenced by grinding parameters and ultrasonic vibration parameters. So, the dividing line defined in Sect. 3.5.3 is introduced into this section. Then, similar to grinding region 2, all the abrasives in grinding region 3 are considered to be evenly spaced and distributed around the circumferences according to equally spaced radius. The outermost layer is defined as the 1_{st} circumference. As shown in Fig. 10, $\theta_{1,1,3}$ is defined as the rotation angle of the first abrasive in the 1_{st} circumference, and the difference between the rotation angles of the first abrasives of adjacent tow circumferences is defined as $\triangle\theta_{1,3}$. The rotation angle of the first grain in j_{th} circumference is defined as $\theta_{j,1,3}$.

$$\theta_{1,1,3}=\pi-\arcsin\left(\frac{r_s-L_2}{r_s}\right) \tag{105}$$

$$\Delta\theta_{1,3}=\frac{\left(\theta_{1,1,3}-{}^{\pi}/_{2}\right)}{n_L} \tag{106}$$

$$\theta_{j,1,3}=\theta_{1,1,3}-(j-1)\Delta\theta_{1,3} \tag{107}$$

In grinding region 3, the arc length of the j_{th} circumference is defined as $L_{j,3}$ and its corresponding central angle is defined as $\theta_{j,3}$. The grain number of the abrasives in the j_{th} circumference is defined as $n_{j,3}$.

$$\theta_{j,3}=\pi+2\left(\pi-\theta_{j,1,3}\right) \tag{108}$$

$$L_{j,3}=\theta_{j,3}\pi r_s \tag{109}$$

$$n_{j,3}=C_s L_{j,3} \tag{110}$$

The difference between the rotation angles of adjacent abrasives in the j_{th} circumference is defined as $\triangle\theta_{j,3}$. The rotation angle of the i_{th} abrasive in the j_{th} circumference is defined as $\theta_{j,i,3}$.

$$\Delta\theta_{j,3}=\frac{\theta_{j,3}}{n_{j,3}} \tag{111}$$

$$\theta_{j,i,3}=\theta_{j,1,3}+(i-1)\Delta\theta_{j,3},\quad i\in\left(1,n_{j,3}\right),\ \ \theta_{j,i,3}\in\left(\theta_{j,1,3},3\pi-\theta_{j,1,2}\right) \tag{112}$$

The tangential force, normal force, and radial force of the i_{th} abrasive in the j_{th} circumference are defined, respectively, as $F_{ci,gs3}$, $F_{ni,gs3}$, and $F_{ri,gs3}$. Then, the component forces of total force along normal direction and y axis direction in grinding region 3 can be expressed as

$$F_{n,s3}=\sum_{j=1}^{n_l}\sum_{i=1}^{n_{j,3}}F_{ni,gs3} \tag{113}$$

$$F_{y,s3}=\sum_{j=1}^{n_L}\sum_{i=1}^{n_{j,3}}F_{ci,gs3}\sin\theta_{j,i,3} \tag{114}$$

Due to the symmetry of grinding region 3, the resultant force in axis direction of single-grinding forces of all abrasives in this grinding region is equal to zero, namely,

$$F_{x,s3}=0 \tag{115}$$

where $F_{n,s3}$, $F_{n,s3}$, and $F_{n,s3}$ are, respectively, the component forces of total grinding force in grinding region 3 along normal direction, x axis direction, and y axis direction.

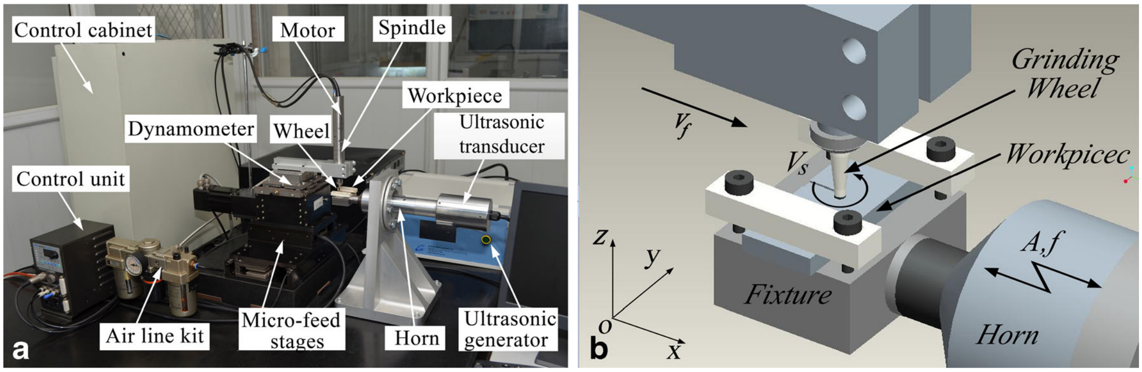

Fig. 11 Experimental setup. **a** The machine tool and **b** amplified drawings

3.5.5 Total grinding force modeling

As analyzed above, three component forces of the total grinding fore of all abrasive in main grinding zone, plowing zone, and sliding zone have been established, respectively. Based on vector addition theory, the component forces of the total grinding force of the wheel along normal direction, *x* direction, and *y* direction can be expressed as

$$F_n = F_{n,1} + F_{n,p2} + F_{n,s3} \tag{116}$$

$$F_x = F_{x,g1} \tag{117}$$

$$F_y = F_{y,g1} + F_{y,gp2} + F_{y,gs3} \tag{118}$$

4 Experimental details

4.1 Experimental machine tools

The ultrasonic vibration-assisted micro-end grinding of silica glass is conducted on a manual-developed machine tool, as shown in Fig. 11, which is built for the purpose of realization of the following three crucial motions in UAMEG: workpiece ultrasonic vibration, high-speed grinding wheel rotation, and high-accuracy feed motion.

Ultrasonic vibration of the silica glass sample, which actually is reciprocation harmonic motion with high frequency and low amplitude, is created by a piezoelectric actuator with input of sine voltage signal derived from an ultrasonic generator. The vibration amplitude is amplified by a specially designed acoustical waveguide booster to attain desirable vibration amplitude values on sample. The silica glass sample is adhered and fixed onto a fixture, which is designed to be minimum dimension and weight to limit distortion of ultrasonic waveform and loss of ultrasonic energy. Ultrasonic vibration of the sample with tunable amplitudes (from 3 to 8.5 μm) at 20-kHz frequency can be achieved by changing input power from 0.2 to 0.8 kW.

High-speed and reliable rotating motion of micro-diamond grinding wheel is created by a high-performance spindle system. The micro-electroplated diamond grinding wheel (radius 1000 μm) is installed on a high-speed spindle (up to 50,000 rpm) with high spindle accuracy (within 1 μm).

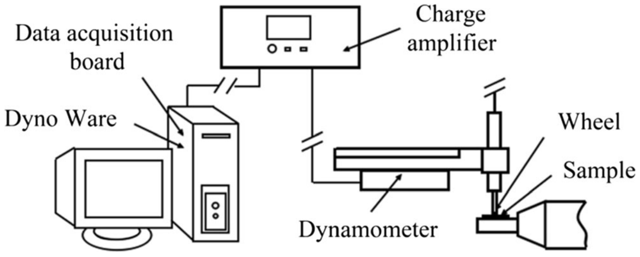

Fig. 12 Schematic of force measurement instrument

Table 1 Design of experimental conditions of end grinding tests

Experiment no.	A (μm)	n (r/min)	a_p (μm)	v_w (μm/s)
1	0	18,000	2	100
2	6.5	18,000	2	100
3	7.5	18,000	2	100
4	8.5	18,000	2	100
5	8.5	8,000	2	100
6	8.5	27,000	2	100
7	8.5	36,000	2	100
8	8.5	18,000	1.5	100
9	8.5	18,000	2.5	100
10	8.5	18,000	1	100
11	8.5	18,000	1	40
12	8.5	18,000	1	70
13	8.5	18,000	1	130
14	0	8,000	2	100
15	0	27,000	2	100
16	0	36,000	2	100
17	0	18,000	1.5	100
18	0	18,000	2.5	100
19	0	18,000	1	100
20	0	18,000	1	40
21	0	18,000	1	70
22	0	18,000	1	130

High-accuracy micro-feed motion is created by a triaxial micro-feed system. It is assembled with two precision grade linear motor horizontal stages with 3-μm position accuracy and ±0.4-μm bidirectional repeatability and a precision grade servo motor vertical stage resolution with ±1-μm accuracy and ±0.75-μm bidirectional repeatability.

A three-component force dynamometer unit (Kistler 9256-C2) is used for the measurement of the grinding forces, as shown in Fig. 12. The grinding forces generated in grinding zone are to be converted into charge signal by the piezoelectric dynamometer. The multi-channel charge amplifier receives the charge signal from the dynamometer and converts it into a proportional voltage. The built-in

Table 2 Material properties of silica glass sample

Property name	Value
Hardness (GPa)	6.2
Young's modulus (GPa)	820×10^3
Fracture toughness (MPa/m$^{1/2}$)	1.2

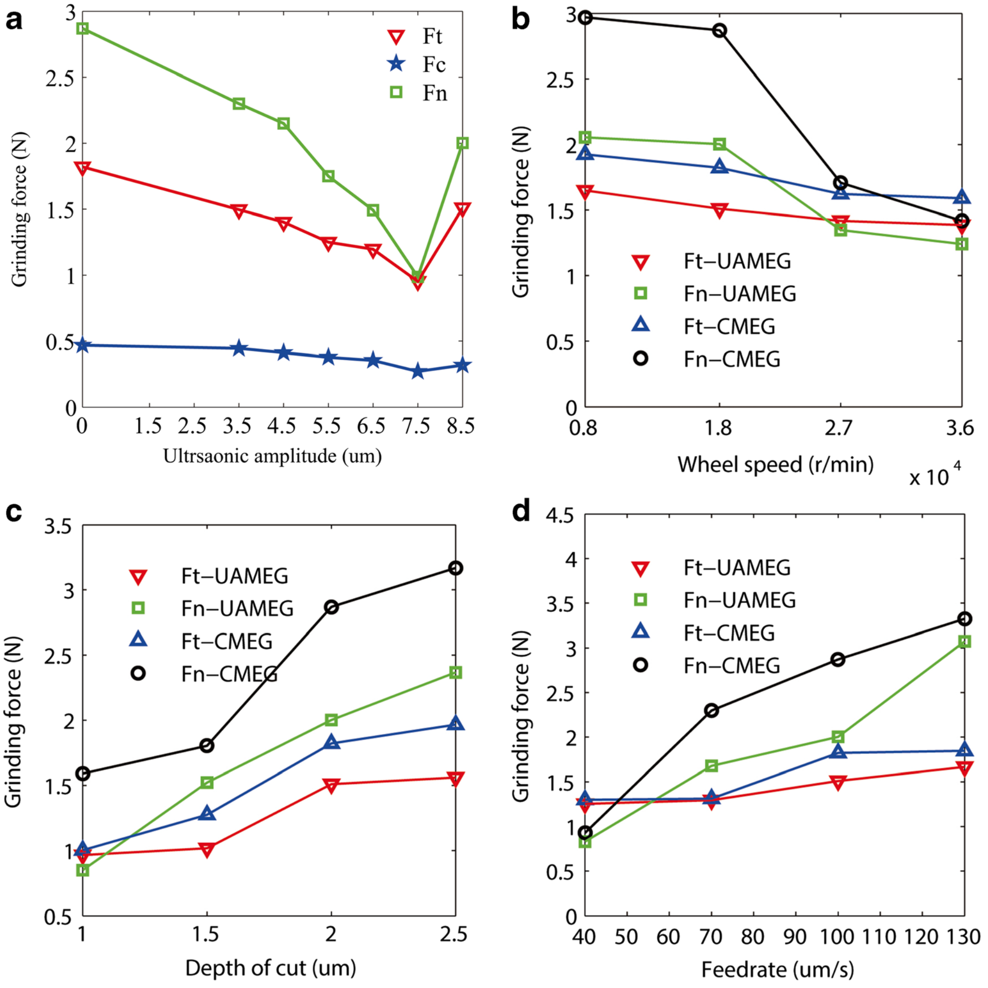

Fig. 13 Effects of ultrasonic amplitude and grinding parameters on grinding forces. **a** Effects of ultrasonic amplitude ($v_w = 100$ μm/s, $a_p = 2$ μm, $n = 18{,}000$ r/min). **b** Effects of wheel speed ($v_w = 100$ μm/s, $a_p = 2$ μm, $A = 8.5$ μm). **c** Effects of depth of cut ($v_w = 100$ μm/s, $n = 18{,}000$ r/min, $A = 8.5$ μm). **d** Effects of wheel feed rate ($a_p = 2$ μm, $n = 18{,}000$ r/min, $A = 8.5$ μm)

high-pass filter is used to filtering interference signal from spindle rotation. A data acquisition and analysis system (DynoWare) are used for data collection and display.

4.2 Experimental conditions and process

To investigate particularly and contrastively the influence of aided ultrasonic vibration and grinding parameters on variation tendency of grinding forces and surface characteristics, the single-factor experiment is set up and the experimental grinding parameters are shown in Table 1. The size of the silica glass sample is 50 × 20 × 3 mm, and its material properties are shown in Table 2. The radius and grain size of electroplated diamond grinding wheel are, respectively, 1.5 mm and no. 270. To minimize the influence of parallelism error of wheel end face and sample surface, the experimental system is adjusted using a gradienter during assembling and clamping process, and repeated fine grinding is conducted on sample surface before every recorded test.

5 Results and discussion

5.1 Influence of ultrasonic vibration and grinding parameters on grinding forces

In this section, according to the experimental parameters in Table 1, contrastive experiments with and without ultrasonic

Table 3 Variation percentage of the grinding forces with/without ultrasonic assistance

Experiment no.	Variation percentage (%)		
		UAMEG	CMEG
Wheel speed	F_n	−39.6	−52.3
	F_t	−15.9	−17.4
Depth of cut	F_n	179.0	99.2
	F_t	61.9	96.2
Feed rate	F_n	270.5	258.3
	F_t	32.9	42.0

Table 4 Material properties of Al_2O_3

E (GPa)	HV	HB	K_{IC} (MPa/m$^{1/2}$)	G (GPa)	b (10^{-10} m)	T_{melt}	T_0
121	650	618	≥4.8	109.7	0.471	2050 °C	20 °C

vibration is conducted. According to the result of grinding force measuring and machining surface micro-structure, the influence of machining parameters on grinding force and surface micro-structure and intermittent cutting condition are analyzed.

Figure 13a shows the grinding forces in contrastive experiments with and without ultrasonic vibration under the grinding conditions of $n = 1.8 \times 10^4$ r/min, $a_p = 2$ μm, and $v_w = 100$ μm/s, of which F_n, F_t, and F_c denote the normal, tangential, and cross-feed directional grinding forces, respectively. It can be seen that the normal grinding force and the tangential grinding force in experiments with ultrasonic vibration are much less than those in experiments without ultrasonic vibration, and approach the minimum value at ultrasonic amplitude of 7.5 μm, and then increase with ultrasonic amplitude increasing to 8.5 μm. The influence of ultrasonic assistance on cross-feed direction is relatively smaller.

Figure 13b shows the varying trends of normal and tangential grinding forces under different wheel speeds in both UAMEG and conventional micro-end grinding (CMEG). When wheel speed increases from 8000 to 36,000 r/min, the normal grinding force decreases rapidly, while the tangential grinding force decreases smoothly. When grinding wheel speed increases, the instantaneous abrasive cutting thickness becomes smaller, so the individual abrasive force is reduced as well as the total grinding force.

Figure 13c shows the varying trends of normal and tangential directional grinding forces under different depths of cut in both UAMEG and CMEG. The normal grinding force and the tangential grinding force increase with the depth of cut increasing from 1 to 2.5 μm. When the depth of cut increases, the instantaneous abrasive cutting thickness is unchanged, but effective rake angle of grains and the undeformed cutting thickness increase, which leads to the increasing of the grinding forces.

Figure 13d shows the varying trends of normal and tangential directional grinding forces under different feed rates in both UAMEG and CMEG. The normal grinding force and the tangential grinding force increase smoothly with the feed rate increasing from 40 to 130 μm/s. Because the feed rate increases, the instantaneous abrasive cutting thickness and the abrasive-workpiece contact area increase, which leads to the increasing of the individual abrasive force and the total grinding force.

Table 5 Properties of TC4 in Johnson-Cook material model

A (MPa)	B (MPa)	C	m	n
862.5	331.2	0.012	0.8	0.34

It is indicated from Table 3 that the variation percentages of tangential grinding force with increase of wheel speed, depth of cut, and feed rate in UAMEG are smaller than in CMEG. The variation percentages of normal grinding forces with increase of wheel speed and feed rate in UAMEG are larger than in CMEG; meanwhile, the variation percentage with increase of wheel speed in UAMEG is smaller than in CMEG. It can be concluded that aided ultrasonic vibration weakened the effect of increase of wheel speed on variation percentage of normal grinding force but strengthens the effect of increase of depth of cut and feed rate. The aided ultrasonic vibration enhances the effect of increase of all the three grinding parameters on variation tangential grinding force.

5.2 Comparison of model predicted values and the experimental values

The UAMEG experiments are conducted with Al_2O_3 silica glass sample. According to force modeling of Eqs. (119)–(121), the simulation calculation is achieved under the same machining parameters. The undetermined coefficient values are obtained by experimental data, $\mu_0 \approx 2 \times 10^6$, $\chi \approx 1.9 \times 10^{10}$, and $C_{Oxley} \approx 4.6 \times 10^8$. To verify the correctness of the established model, the model calculation results and the experimental measured results are contrastively analyzed. The size of the silica glass sample is 50 × 20 × 3 mm, and its property parameters are shown in Table 4. The hard alloy TC4 Johnson-Cook material constitutive model parameter is adopted to

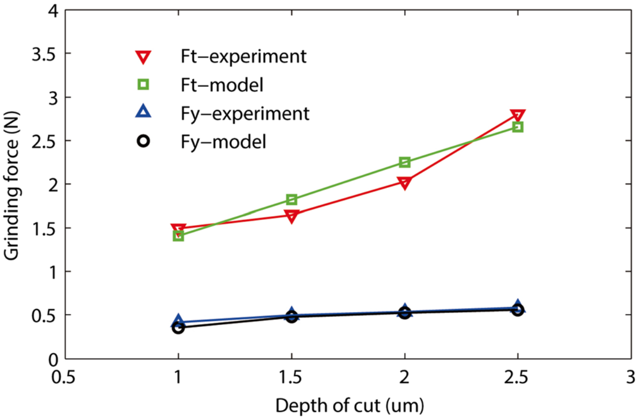

Fig. 14 Contrast diagram of grinding forces under different grinding depth ($v_w = 100$ μm/s, $n = 18,000$ r/min, $A = 8.5$ μm)

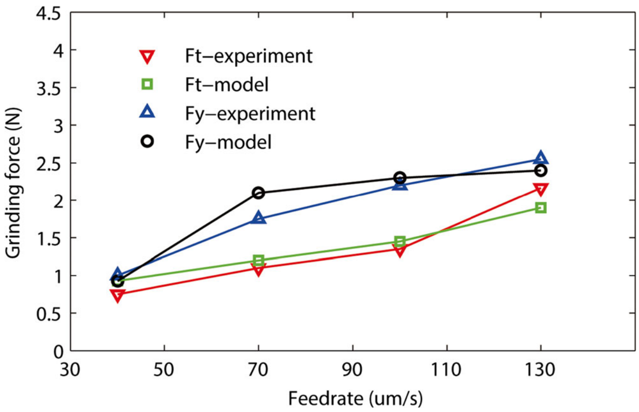

Fig. 15 Contrast diagram of grinding forces under different feed rate ($a_p = 2$ μm, $n = 18{,}000$ r/min, $A = 8.5$ μm)

approximately characterize the micro-scale plastic properties of alumina ceramic materials in the main grinding zone, as shown in Table 5.

$$F_n^{'} = (F_n C_{n1} + C_{n2}) C_{n3} \tag{119}$$

$$F_x^{'} = (F_x C_{x1} + C_{x2}) C_{x3} \tag{120}$$

$$F_y^{'} = \left(F_y C_{y1} + C_{y2}\right) C_{y3} \tag{121}$$

As shown in Fig. 14, the model calculation results match well with the experimental results when the tangential grinding force and cross-feed directional grinding force increase with the increase of depth of cut when depth of cut increases from 1 to 2.5 μm. When the depth of cut increases, the instantaneous abrasive cutting thickness is unchanged, but it will lead to increasing of effective rake angle of grains and the undeformed cutting thickness. Hence, grinding force increases.

As shown in Fig. 15, when feed rate increases from 40 to 130 μm/s, the model calculation results of the normal grinding force and the tangential grinding force match well with experimental results; both showed a trend of gradual increase, and the normal grinding force increases smoothly. When the feed rate increases, the instantaneous abrasive cutting thickness and the contact area of abrasive-workpiece increase. So, the individual abrasive force and the total grinding force increase.

6 Conclusion

In this paper, an analytical model for predicting grinding force considering size effect in UAMEG of silica glass is built, and the experimental study is conducted to finally establish and verify the proposed model. The conclusions are as follows:

According to the micro-topography of grinding surface, the grinding zone between the wheel and material in micro-end grinding is split into the following three grinding regions: chip formation region, plowing region, and sliding region, and the material removal mechanism under the three grinding regions is investigated systematically.

Based on the different material removal modes and undeformed chip thickness, the single-grain force model is developed. Considering the size effect and the random distribution of abrasives on grinding wheel, the grinding force model of the whole grinding wheel is established. This model is validated by the experimental results of silica glass in UAMEG.

The grinding tests of silica glass using micro-radial electroplated diamond wheel are conducted. The experiment results demonstrate that the grinding forces are significantly reduced. The predicted and the measured values of grinding force are in very good agreement.

Acknowledgments This work was supported by the Natural Science Foundation of Hebei Province of China (project numbers E2012202088 and E2012202112) and Innovation Fund for Outstanding Youth of Hebei University of Technology (project number 2012011).

References

1. Zhong ZW, Venkatesh VC (2009) Recent developments in grinding of advanced materials. Int J Adv Manuf Technol 41:468–480
2. Sreejith PS, Ngoi BKA (2001) Material removal mechanisms in precision machining of new materials. Int J Mach Tools Manuf 41:1831–1843
3. Liu K, Li XP, Liang SY (2007) The mechanism of ductile chip formation in cutting of brittle materials. Int J Adv Manuf Technol 33:875–884
4. Ramesh K, Huang H, Yin L, Zhao J (2004) Microgrinding of deep micro grooves with high table reversal speed. Int J Mach Tools Manuf 44:39–49
5. Perveen A, Jahan MP, Rahman M, Wong YS (2012) A study on microgrinding of brittle and difficult-to-cut glasses using on-machine fabricated poly crystalline diamond (PCD) tool. J Mater Process Technol 212:580–593
6. Dornfeld D, Min S, Takeuchi Y (2006) Recent advances in mechanical micromachining. CIRP Ann Manuf Technol 55:745–768
7. Feng J, Kim BS, Shih A, Ni J (2009) Tool wear monitoring for micro-end grinding of ceramic materials. J Mater Process Technol 209:5110–5116
8. Akbari J, Borzoie H, Mamduhi MH (2008) Study on ultrasonic vibration effects on grinding process of alumina ceramic (Al_2O_3). World Acad Sci Eng Technol 41:785–789
9. Tawakoli T, Azarhoushang B, Rabiey M (2009) Ultrasonic assisted dry grinding of 42CrMo4. Int J Adv Manuf Technol 42:883–891
10. Chen HF, Tang JY, Zhou W (2013) An experimental study of the effects of ultrasonic vibration on grinding surface roughness of C45 carbon steel. Int J Adv Manuf Technol 68:2095–2098
11. Yan YY, Zhao B, Liu JL (2009) Ultraprecision surface finishing of nano-ZrO_2 ceramics using two-dimensional ultrasonic assisted grinding. Int J Adv Manuf Technol 43(5–6):462–467
12. Wang Y, Lin B, Wang SL, Cao XY (2014) Study on the system matching of ultrasonic vibration assisted grinding for hard and brittle materials processing. Int J Mach Tools Manuf 77:66–73
13. Zhang JH, Zhao Y, Zhang S, Wei Z (2014) Kinematic analysis of ultrasonic vibration assisted micro end grinding. Key Eng Mater 609:1357–1361

14. Zhang JH, Zhao Y, Zhang S, Tian FQ, Guo LS, Dai RZ (2014) Study on effect of ultrasonic vibration on grinding force and surface quality in ultrasonic assisted micro end grinding of silica glass. Shock Vib 2014:1–10
15. Hecker R, Ramoneda I, Liang S (2003) Analysis of wheel topography and grit force for grinding process modelling. J Mater Process Technol 5:13–23
16. Park HW, Liang SY (2008) Force modeling of micro-grinding incorporating crystallographic effects. Int J Mach Tools Manuf 48: 1658–1667
17. Chang H, Wang J (2008) A stochastic grinding force model considering random grit distribution. Int J Mach Tools Manuf 48:1335–1344
18. Durgumahanti US, Singh V, Rao PV (2010) A new model for grinding force prediction and analysis. Int J Mach Tools Manuf 50:231–240
19. Agarwal S, Rao PV (2013) Predictive modelling of force and power based on a new analytical undeformed chip thickness model in ceramic grinding. Int J Mach Tools Manuf 65:68–78
20. Cheng J, Gong YD (2014) Experimental study of surface generation and force modeling in micro-grinding of single crystal silicon considering crystallographic effects. Int J Mach Tools Manuf 77:1–15
21. Marshall DB, Lawn BR (1986) Indentation of brittle materials, microindentation techniques in materials science and engineering. ASTM STP 889:26–46
22. Lawn BR, Marshall DB (1979) Hardness, toughness, and brittleness: an indentation analysis. J Am Ceram Soc 62:347–350
23. Arif M, Rahman M, San WY (2011) Analytical model to determine the critical feed per edge for ductile–brittle transition in milling process of brittle materials. Int J Mach Tools Manuf 51:170–181
24. Bolshakov APGM (1998) Influences of pileup on the measurement of mechanical properties by load and depth sensing indentation techniques. J Mater Res 13:1049–1058
25. Malekian M, Mostofa MG, Park SS, Jun MBG (2012) Modeling of minimum uncut chip thickness in micro machining of aluminum. J Mater Process Technol 212:553–559
26. Hill R, Storakers B, Zdunek AB (1989) A theoretical study of the Brinell hardness test. Proc R Soc Lond A Mater 423:301–330
27. Taljat B, Pharr GM (2004) Development of pile-up during spherical indentation of elastic–plastic solids. Int J Solids Struct 41:3891–3904
28. Norbury AL, Samuel T (1928) The recovery and sinking-in or piling-up of material in the Brinell test, and the effects of these factors on the correlation of the Brinell with certain other hardness tests. J Iron Steel Res Int 117:673–687
29. Peng Z, Gong J, Miao H (2004) On the description of indentation size effect in hardness testing for ceramics: analysis of the nanoindentation data. J Eur Ceram Soc 24:2193–2201
30. Gauthier C, Lafaye S, Schirrer R (2001) Elastic recovery of a scratch in a polymeric surface: experiments and analysis. Tribol Int 34:469–479
31. Arcona C, Dow TA (1998) An empirical tool force model for precision machining. J Manuf Sci E-T Asme 120:700–707
32. Perveen A, Rahman M, Wong YS (2014) Modeling and simulation of cutting forces generated during vertical micro-grinding. Int J Adv Manuf Technol 71:1539–1548
33. Park HW (2008) Development of micro-grinding mechanics and machine tools. Georgia Institute of Technology, Atlanta
34. Lai XM, Li HT, Li CF, Lin ZQ, Ni J (2008) Modelling and analysis of micro scale milling considering size effect, micro cutter edge radius and minimum chip thickness. Int J Mach Tools Manuf 48: 1–14
35. Josh SS, Melkote SN (2004) An explanation for the size-effect in machining using strain gradient plasticity. J Manuf Sci E-T Asme 126:679–684
36. KC J (2004) Mechanism of the chip formation and cutting dynamic of the micro scale milling process. University of Michigan, Michigan
37. Oxley PLB, Young HT (1989) The mechanics of machining: an analytical approach to assessing machinability. Ellis Horwood Publisher, London, pp. 136–182
38. Hecker RL (2002) Part surface roughness modeling and process optimal control of cylindrical grinding. Georgia Institute of Technology, Atlanta